Microscale mechanical property variations of Al-substituted LLZO: insights from compression testing and molecular dynamics simulations

Supporting Information

Authors: Jaron V. Moon[a], Md Takmil Sakir[c], Wooseok Go[b,] Rui Xie[a], Michael C. Tucker[b], Marca Doeff[b], Haoran Wang[c], Roseanne Warren[a*]

a. University of Utah, Department of Mechanical Engineering, 1495 E 100 S, Salt Lake City, UT 84112
b. Energy Storage and Distributed Resources Division, Lawrence Berkeley National Laboratory, Berkeley, CA 94720
c. Mechanical and Aerospace Engineering, Utah State University, Logan, UT 84322

* Corresponding Author – roseanne.warren@utah.edu

LLZO Mechanical Properties Literature Comparison

Table S1. Comparison of Al-substituted LLZO mechanical property measurements.

LLZO sample type	Relative density (%)	Test method	Young's modulus (GPa)	Hardness (GPa)	Compressive strength (GPa)	Ref.
Microscale	100 [(a)]	Pillar compression	151	10.07 [(c)]	2.63	This work
	84 [(b)]	Pillar compression	106	7.07 [(c)]	1.43	
Bulk	96	Nanoindentation (Berkovich tip)	145	11.1	-	
	93	Nanoindentation (Berkovich tip)	145.6	8.5	-	[1][(d)]
	>98	Nanoindentation (Berkovich tip)	150.3	-	-	[2]
	97	Vickers hardness	149.8	6.3	-	[3]
	98	Vickers hardness	-	9.1	-	[4] [(e)]

(a) The relative density of a "pristine" pillar is assumed to be 100%.

(b) Estimated from Equation 2 for a porous pillar.

(c) Estimated given $H = \frac{E(1-2v)}{6+6v}$, where $v = 0.25$.

(d) Also reports fracture toughness values of 0.99 MPa*m$^{1/2}$ and 1.19 MPa*m$^{1/2}$ from micro-pillar splitting and VIF fracture toughness, respectively.

(e) Also reports a fracture toughness value of 0.97 MPa*m$^{1/2}$ from VIF fracture toughness crack length measurements.

Table S2. Comparison of Al-substituted LLZO ionic conductivity measurements.

LLZO sample type	Relative Density (%)	Ionic Conductivity (mS/cm)	Reference
Bulk	93	0.021	[1]
	96	0.13	This work
	98	0.34	[4]
	>98	0.4	[2]

Molecular Dynamics Simulations

To model crystalline LLZO, we employed the Buckingham-Coulomb interatomic potential, which accounts for ionic bonds through the representation of short-range nuclear repulsion and long-range Coulombic attraction-repulsion (Equation S1) [5]:

$$U_{ij} = \frac{q_i q_j}{4\pi\varepsilon|r_{ij}|} + A_{ij}\, exp(-B_{ij}\,|r_{ij}|) - \frac{C_{ij}}{|r_{ij}|^6} \quad \text{(S1)}$$

where r_{ij} represents the distance between atom i and atom j, and ε is vacuum permittivity [5]. The effective charges of i and j are denoted as q_i and q_j, respectively. The constants A_{ij}, B_{ij} and C_{ij} are empirical values. The potential parameters, as obtained from [6], are detailed in Table S3.

Table S3. Interatomic potential parameters used in MD simulations.

Atom i	Atom j	A_{ij} (eV)	B_{ij} (Å^{-1})	C_{ij} (eV Å^6)	q_i	q_j
Al	O	7042.59	4.316	101.50	2.1	-1.4
Li	O	876.86	3.863	0.00	0.7	-1.4
La	O	14509.63	4.102	30.83	2.1	-1.4
Zr	O	2153.80	3.439	0.00	2.8	-1.4
O	O	4869.99	4.163	27.22	-1.4	-1.4

This potential reproduces cell parameters precisely for both phases [5]. To fix the problems of collision of atoms with Buckingham-Coulomb potentials, known as Buckingham catastrophe [5], we used the correction term suggested by [5]. The final potential energy between atoms with correction term is given by Equation S2:

$$U_{ij} = \frac{q_i q_j}{4\pi\varepsilon|r_{ij}|} + A_{ij}\, exp(-B_{ij}\,|r_{ij}|) - C_{ij}\, r_{ij}^{-6} + D_{ij}\, r_{ij}^{-12} \quad \text{(S2)}$$

where the last term is added as a remedy, using $D_{ij} = C_{ij}$, so that atoms on the surfaces do not collide with each other [5]. We compared the stress-strain response of Al-substituted LLZO with this correction term to the response without this term. It was found that using this term had a negligible effect on the stress-strain response.

SRIM Modeling

SRIM modeling was completed using the TRIM calculation for ion distribution and setting the layer to the Al-substituted stoichiometry ($Li_{6.25}Al_{0.25}La_3Zr_2O_{12}$) with a layer density of 4.91 g/cm^3. A 50 nm layer thickness was used to accurately estimate ion depth and for visualization purposes. The ion data was set to a gallium ion with an accelerating voltage of 30 keV. The angle of incidence was set to 0° (lower bound) and 89° (upper bound) to extract to what extent ion implantation may occur. The total number of ions interacting with the surface was set to 3000. The authors recognize that the SRIM modeling does not take into account material removal during ion implantation, a time step, or the true angle of the material interacting with the beam but provides a good indication of the ion beam effect on material composition.

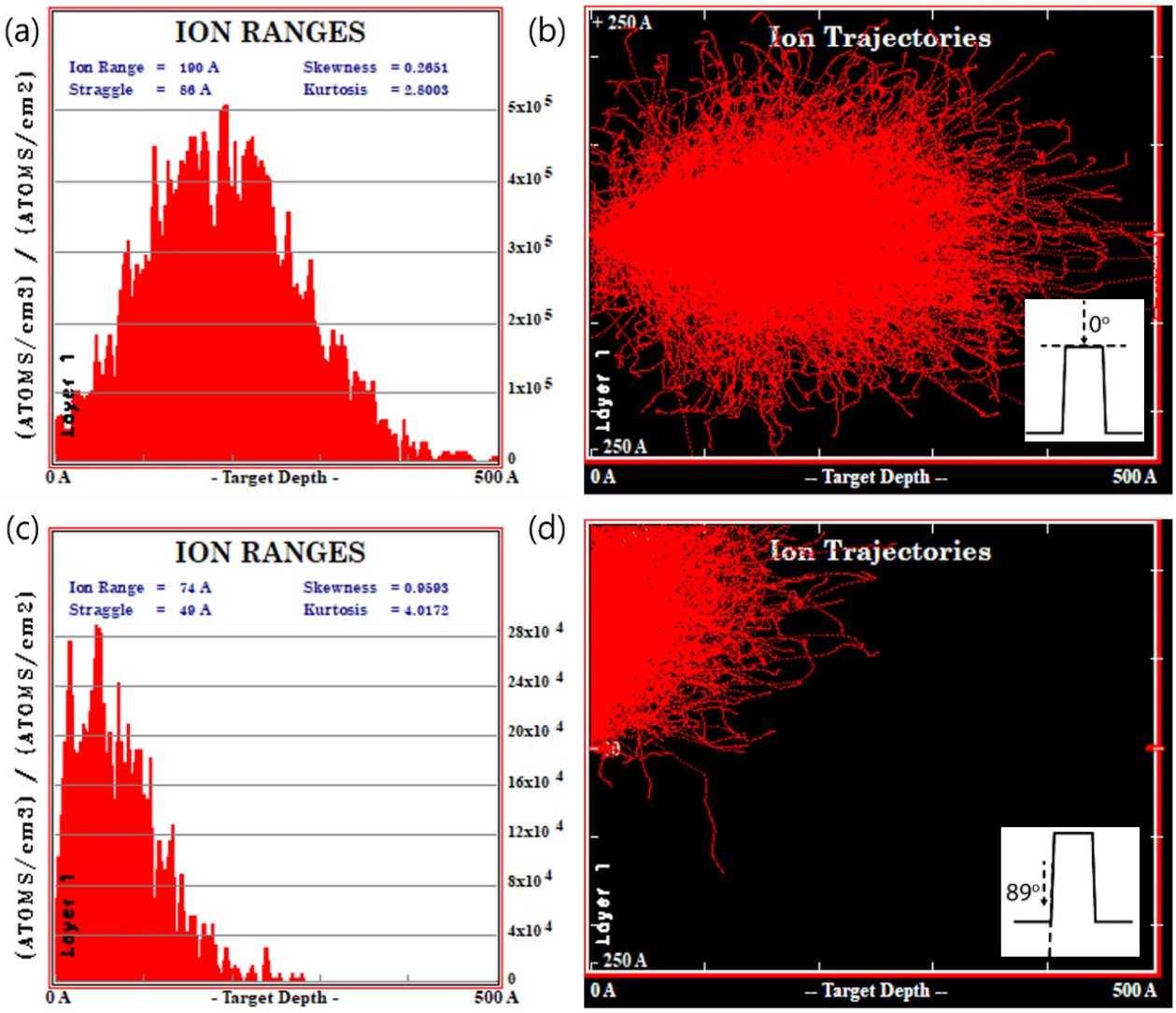

Figure S1. SRIM modeling results of gallium ion implantation. a) Normal distribution of ion implantation at 0° incident angle. b) Ion trajectories into Al-substituted LLZO with a 0° incident angle. c) Normal distribution of ion implantation at 89° incident angle. d) Ion trajectories into Al-substituted LLZO with an 89° incident angle.

Pile-up Correction of LLZO

Nanoindentation of LLZO exhibits features of pile-up during indentation (Figure 3g). Pile-up causes an overestimation of the area tip function, resulting in an overestimate of Young's modulus and hardness. A pile-up correction was performed by averaging pile-up heights from all three sides of the indenter. The contact area was then corrected, as presented in [7]. Pile-up height measurements were taken using the scanning probe microscopy application on the nanoindenter. Before correction, indentation estimated a Young's modulus and hardness value of 169.7 and 12.4 GPa, respectively. After a correction was applied the Young's modulus and hardness were corrected to and reported as 145 and 11.1 GPa, respectively.

Young’s Modulus Calculation

Table S4 provides statistical results for two-way t-tests of Young's modulus values calculated from pillar compression experiments by three methods: 1) average slope of the linear elastic region of the unloading stress-strain curve before failure; 2) slope of the linear elastic region of the stress-strain curve loaded to failure, and 3) by the equation presented in Yang *et al.* [8] (Equation 1 in manuscript). Some pillars failed at a much lower stress than anticipated; those pillars' Young’s modulus values are not estimated by averaging of the unloading curves. Two-sided t-tests assuming unequal variance show that the results from the different methods are not statistically different (Table S4).

Table S4. Statistical results for two-way t-tests assuming unequal variance.

	Method 3 vs. 2	Method 1 vs. 3	Method 1 vs. 2
df	26	22	20
t stat	-1.233	-0.472	0.9874
P value	0.2287	0.6419	0.3352
t critical	2.056	2.074	2.086

Rate Dependency

Ceramic materials may show rate dependency during compression testing [9], which is due to loading occurring quicker than crack propagation can occur. Within this work, it was found that both the measured Young's modulus and compressive strength show no rate dependency when the loading rate is between 100 µN/s and 3500 µN/s (nominal strain rates ranging from ~0.1 s^{-1} to 0.01 s^{-1}) (Figure S2). A regression model was used to determine the statistical significance of the effect of rate dependency on both the Young's modulus and compressive strength, where statistically, no correlation is shown ($F_{1,12} = 0.95$, $p = 0.35$), ($F_{1,12} = 2.63$, $p = 0.13$).

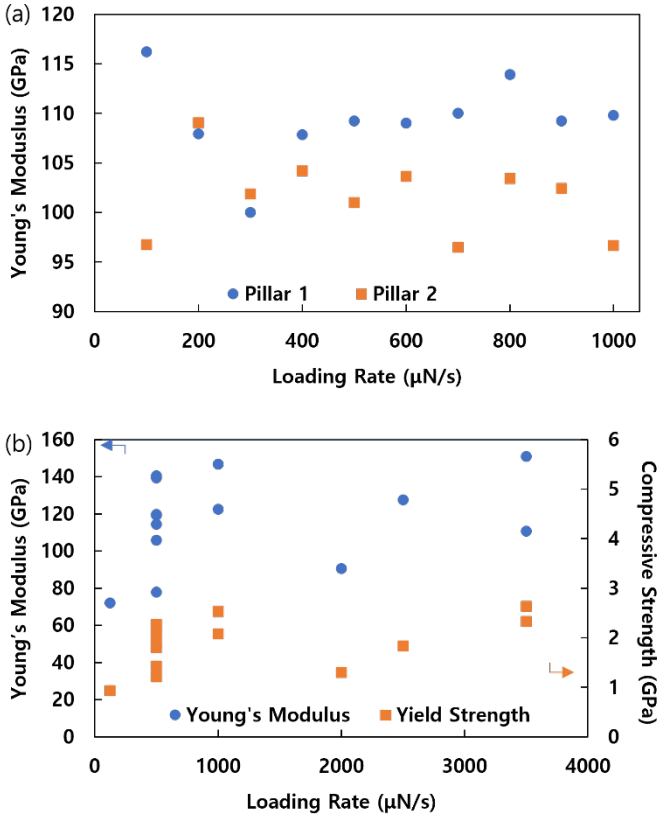

Figure S2. Rate dependency study of LLZO pillar compression. a) Two samples measured with varying loading rates to show no change in Young's modulus. b) All pillars' Young's modulus and compressive strength values plotted against the loading rate.

Relation of Pillar Failure to Location

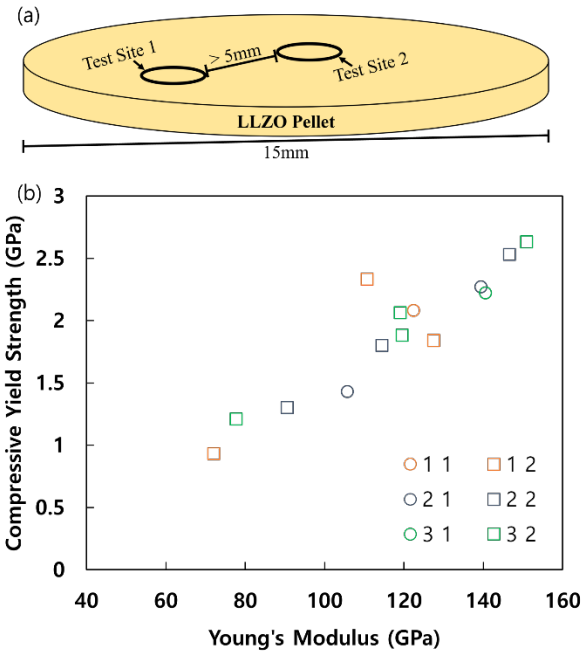

Figure S3. Pillar location for each pillar compressed until failure. a) Schematic of an LLZO pellet with test sites indicated. b) Compressive strength vs. Young's modulus, with data points distinguished by pellet number and testing location number. Data point label '1 2' denotes pillars from pellet one at test site two.

FIB Cross-Sectional Imaging of LLZO

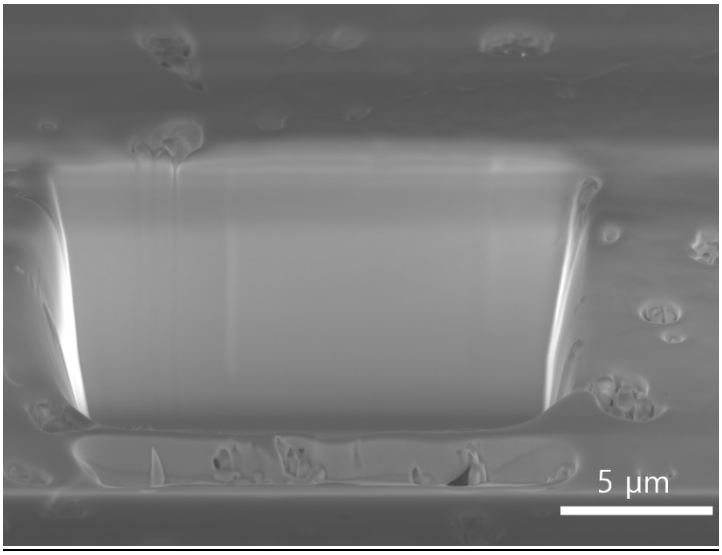

Figure S4. FIB milled trench on LLZO pellet. No internal defects are introduced after FIB milling, as shown by the clean internal structure.

SEM Images of Fractured LLZO Pillars

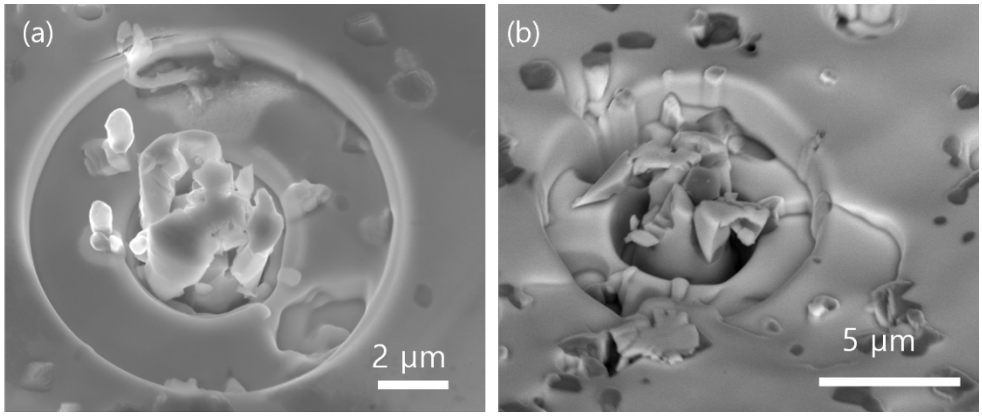

Figure S5. Pillar fracture after compression. Both inter- and intragranular fracture is apparent from the SEM images.

LLZO Porosity Distribution

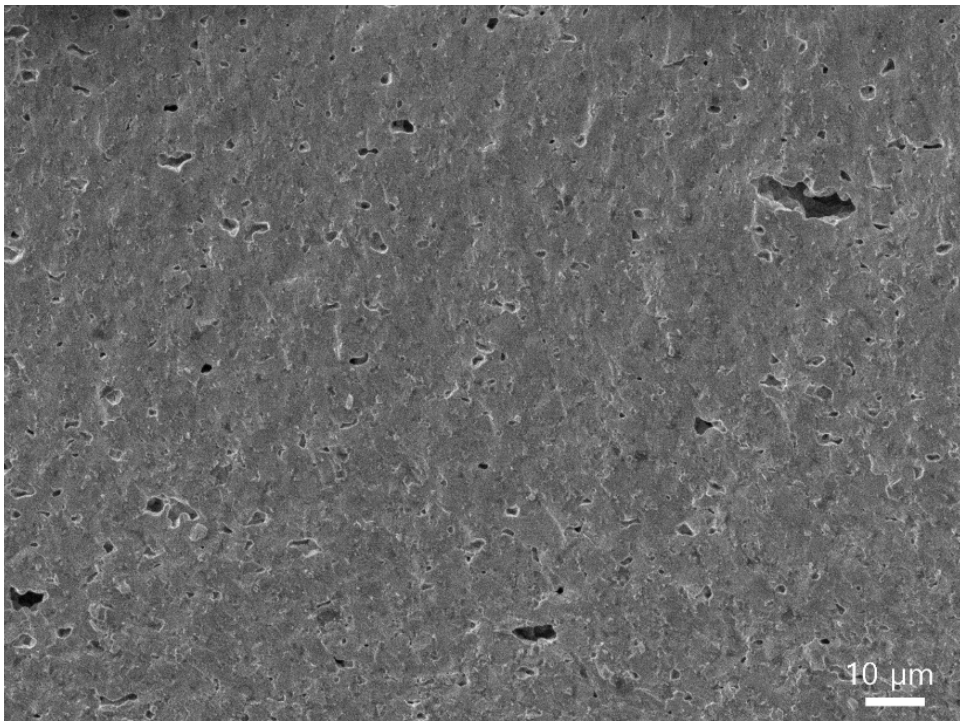

Figure S6. Cross-sectional SEM image of an LLZO pellet. Distributed porosity is apparent through the thickness of the pellet.

References

[1] A. Wang, J. F. Nonemacher, G. Yan, M. Finsterbusch, J. Malzbender, and M. Krüger, 'Mechanical properties of the solid electrolyte Al-substituted Li7La3Zr2O12(LLZO) by utilizing micro-pillar indentation splitting test', *J Eur Ceram Soc*, vol. 38, pp. 3201–3209, 2018, doi: 10.1016/j.jeurceramsoc.2018.02.032.

[2] S. Yu *et al.*, 'Elastic Properties of the Solid Electrolyte Li7La3Zr2O12 (LLZO)', *Chemistry of Materials*, vol. 12, pp. 197–206, 2016, doi: 10.1021/acs.chemmater.5b03854.

[3] J. E. Ni, E. D. Case, J. S. Sakamoto, E. Rangasamy, and J. B. Wolfenstine, 'Room temperature elastic moduli and Vickers hardness of hot-pressed LLZO cubic garnet', *J Mater Sci*, vol. 47, pp. 7978–7985, 2012, doi: 10.1007/s10853-012-6687-5.

[4] Y. Kim, H. Jo, J. L. Allen, H. Choe, J. Wolfenstine, and J. Sakamoto, 'The Effect of Relative Density on the Mechanical Properties of Hot-Pressed Cubic Li 7 la 3 Zr 2 O 12', *Journal of the American Ceramic Society*, vol. 99, no. 4, pp. 1367–1374, Apr. 2016, doi: 10.1111/jace.14084.

[5] G. V. Lewis and C. R. A Catlow, 'Potential models for ionic oxides', *Journal of Physics C: Solid State Physics*, vol. 18, p. 1149, 1985, doi: 10.1088/0022-3719/18/6/010.

[6] S. Monismith, J. Qu, and R. Dingreville, 'Grain-boundary fracture mechanisms in Li7La3Zr2O12 (LLZO) solid electrolytes: When phase transformation acts as a temperature-dependent toughening mechanism', *J Mech Phys Solids*, vol. 160, p. 104791, 2022, doi: 10.1016/j.jmps.2022.104791.

[7] P. Zhu, Y. Zhao, S. Agarwal, J. Henry, and S. J. Zinkle, 'Toward accurate evaluation of bulk hardness from nanoindentation testing at low indent depths', *Mater Des*, vol. 213, p. 110317, 2022, doi: 10.1016/j.matdes.2021.110317.

[8] Y. Yang, J. C. Ye, J. Lu, F. X. Liu, and P. K. Liaw, 'Effects of specimen geometry and base material on the mechanical behavior of focused-ion-beam-fabricated metallic-glass micropillars', *Acta Mater*, vol. 57, pp. 1613–1623, 2009, doi: 10.1016/j.actamat.2008.11.043.

[9] J. D. Hogan, L. Farbaniec, T. Sano, M. Shaeffer, and K. T. Ramesh, 'The effects of defects on the uniaxial compressive strength and failure of an advanced ceramic', *Acta Mater*, vol. 102, pp. 263–272, 2016, doi: 10.1016/j.actamat.2015.09.028.